

TIME-DEPENDENT MULTI-GROUP MULTIDIMENSIONAL RELATIVISTIC RADIATIVE TRANSFER CODE BASED ON SPHERICAL HARMONIC DISCRETE ORDINATE METHOD

NOZOMU TOMINAGA^{1,2}, SANSHIRO SHIBATA^{3,1}, SERGEI I. BLINNIKOV^{4,5,2}

Accepted for publication in the Astrophysical Journal Supplement Series.

ABSTRACT

We develop a time-dependent multi-group multidimensional relativistic radiative transfer code, which is required to numerically investigate radiation from relativistic fluids involved in, e.g., gamma-ray bursts and active galactic nuclei. The code is based on the spherical harmonic discrete ordinate method (SHDOM) that evaluates a source function including anisotropic scattering in spherical harmonics and implicitly solves the static radiative transfer equation with a ray tracing in discrete ordinates. We implement treatments of time dependence, multi-frequency bins, Lorentz transformation, and elastic Thomson and inelastic Compton scattering to the publicly available SHDOM code. Our code adopts a mixed frame approach; the source function is evaluated in the comoving frame whereas the radiative transfer equation is solved in the laboratory frame. This implementation is validated with various test problems and comparisons with results of a relativistic Monte Carlo code. These validations confirm that the code correctly calculates intensity and its evolution in the computational domain. The code enables us to obtain an Eddington tensor that relates first and third moments of intensity (energy density and radiation pressure) and is frequently used as a closure relation in radiation hydrodynamics calculations.

Subject headings: relativistic processes — radiative transfer — shock waves

1. INTRODUCTION

Radiative transfer is an important piece of physics to describe how an astronomical object is observed. Also the radiation often affects dynamical behavior of the astronomical object. Thus it has been studied in many astrophysical fields. However, the radiative transfer equation is intrinsically a 6-dimensional Boltzmann equation that is computationally expensive. Therefore, the radiative transfer equation is frequently solved in a simplified and approximated form appropriate for an object of interest.

Methods for the multidimensional radiative transfer and radiation hydrodynamics are developed in various fields, e.g., cosmological structure formation (e.g., Iliev et al. 2006, 2009, for a review), star formation (e.g., Krumholz et al. 2007; Tomida et al. 2013), a stellar and solar atmosphere (e.g., Asplund et al. 2000; Nordlund et al. 2009), and a terrestrial atmosphere (e.g., Clough et al. 2005; Collins et al. 2006). These methods are optimized for individual research fields and involve various sophisticated physics for individual phenomena, e.g., a chemical network for cosmological structure formation and star formation, fine-structure lines for a stellar and solar atmosphere, and molecular lines and scattering by dust for a terrestrial atmosphere. On the other hand, they ignore terms with higher orders than $\mathcal{O}(v/c)$,

i.e., they assume that a fluid velocity is much slower than the light velocity. This is a commonly-used appropriate assumption to simplify the radiative transfer equation but inapplicable for the radiative transfer in a relativistic flow.

An emission from a relativistic flow recently attracts researchers with the advent of a gamma-ray burst (GRB).⁶ The GRB is a phenomenon emitting γ -ray photons from relativistic jets in a short period and one of the brightest objects in the Universe. The GRBs have been detected in the distant Universe with redshift as high as $z \sim 8.2$ (Tanvir et al. 2009; Salvaterra et al. 2009; $z \sim 9.4$ for a photometric redshift, Cucchiara et al. 2011) and are believed to probe the high- z Universe as well as quasars and galaxies. Furthermore, interestingly, it is observationally exhibited that the γ -ray emission has correlations of spectral peak energy versus isotropic radiation energy (Amati et al. 2002) and spectral peak energy versus peak luminosity (Yonetoku et al. 2004). A correlation between X-ray luminosity at the break time and the break time is also suggested (Dainotti et al. 2008). These correlations make researchers think of that the GRB can be a standardizable candle being detectable at higher redshift than Type Ia supernova (e.g., Amati et al. 2008).

The mechanism of GRB prompt emission and the origin of correlations have been intensively studied. Observationally, many satellites and telescopes report large variations of the prompt emission, for example, spectra with thermal (e.g., Ryde et al. 2010), non-thermal (e.g., Abdo et al. 2009b; Zhang & Pe'er 2009), and high-energy components (e.g., Abdo et al. 2009a; Fan et al. 2013), polarization (e.g., Yonetoku et al. 2011; Uehara et al. 2012), and duration (e.g., ultra-long

¹ Department of Physics, Faculty of Science and Engineering, Konan University, 8-9-1 Okamoto, Kobe, Hyogo 658-8501, Japan; tominaga@konan-u.ac.jp

² Kavli Institute for the Physics and Mathematics of the Universe, The University of Tokyo, 5-1-5 Kashiwanoha, Kashiwa, Chiba 277-8583, Japan

³ Theory Center, Institute of Particle and Nuclear Studies, KEK, 1-1 Oho, Tsukuba 305-0801, Japan; sshibata@post.kek.jp

⁴ Institute for Theoretical and Experimental Physics (ITEP), Moscow 117218, Russia; Sergei.Blinnikov@itep.ru

⁵ VNIIA, 22 Sushchevskaya, 127055 Moscow, Russia

⁶ The emission from a relativistic flow is also interesting for, e.g., active galactic nuclei (AGN).

GRBs, Stratta et al. 2013; Levan et al. 2014). A correlation between optical and γ -ray light curves is also exhibited (e.g., Vestrand et al. 2005; Woźniak et al. 2009; Gorbovskoy et al. 2012). Theoretically, the emission mechanism has been investigated by analytic studies (e.g., Mészáros 2006, and references therein) or numerical studies with various assumptions: e.g., superposing blackbody radiation from a scattering photosphere (Blinnikov et al. 1999; Mizuta et al. 2011; Nagakura et al. 2011; Lazzati et al. 2013),⁷ solving a radiative transfer equation in a spherical steady flow (Beloborodov 2011), transferring photons in a steady flow with a relativistic Monte Carlo method (Giannios 2006; Pe’er 2008; Beloborodov 2011; Ito et al. 2013; Lundman et al. 2013; S. Shibata & N. Tominaga in prep.), and calculating a spherical relativistic radiation hydrodynamics (Tolstov 2005; Tolstov et al. 2013).

In spite of plenty observations and theoretical studies for many years, the mechanism of the GRB prompt emission is still under debate (e.g., Zhang 2014). This is mainly because most of studies is restricted to be qualitative and there are few quantitative studies taking account of a structure of relativistic jets. In order to investigate the GRB prompt emission quantitatively, a multidimensional relativistic radiation hydrodynamics calculation is essentially required. This is because the GRB is a relativistic and multidimensional phenomenon and the radiation, of which energy can dominate the matter energy, closely couples with matter. Therefore, it is necessary to develop a radiative transfer code optimized for the GRBs which fully includes the terms higher than $\mathcal{O}(v/c)$.

Much progress is recently made on the multidimensional radiation hydrodynamics calculation, for example, (1) special relativistic 3-dimensional radiation magnetohydrodynamics (Takahashi et al. 2013; Takahashi & Ohsuga 2013), (2) general relativistic 3-dimensional radiation hydrodynamics (Sądowski et al. 2013), (3) 3-dimensional radiation magnetohydrodynamics (Jiang et al. 2012; Davis et al. 2012; Jiang et al. 2014), (4) relativistic Monte Carlo transport coupled with hydrodynamics (Roth & Kasen 2015), and (5) 3-dimensional special relativistic Boltzmann hydrodynamics (Nagakura et al. 2014). However, the calculations (1) and (2) are based on the M1 closure method, which can treat anisotropic radiation field but not intersecting radiation from various sources. This is not suitable for the GRBs because the material, that is surrounding the relativistic jet, e.g., a cocoon, is hot and emits thermal photons to varying directions. The calculation (3) adopts the variable Eddington tensor (VET) method that can treat intersecting radiation from multiple sources and non-local radiation equilibrium, but ignores terms with orders higher than $\mathcal{O}(v/c)$. Recently, Jiang et al. (2014) implements a radiative transfer code involving time dependence and velocity dependent source terms but the method is still accurate up to $\mathcal{O}(v/c)$. The calculation (4) couples a relativistic Monte Carlo transport method implicitly with hydrodynamics solvers and the calculation (5) is, in particular, adopted for the neutrino transport in a collapsing massive star. Although the calculations (4) and (5) would be applicable for the GRBs, the cal-

culation (4) can involve a noise of the Monte Carlo even with a reducing technique they developed and the calculation (5) is time-consuming and might be difficult to increase the number of mesh points because it involves an inversion of a huge matrix. There are also general relativistic radiative transfer codes to describe emission from surroundings of black holes (e.g., Dexter & Agol 2009; Shcherbakov & Huang 2011). The codes first derive photon geodesic trajectories in curved spacetime and integrate a relativistic radiative transfer equation along the geodesic paths. They also would be applicable for the GRBs. However, they waste time and computational resources because it is only required to calculate the trajectory in the flat spacetime in the GRBs.

In this paper, we develop an implicit time-dependent multi-group multidimensional special relativistic radiative transfer (RRT) code with the mixed-frame approach. The RRT code can calculate an Eddington tensor with the intensity and thus could be the first step to a time-dependent special relativistic multidimensional multi-group radiation hydrodynamics code optimized for the GRBs. The RRT code is based on the spherical harmonic discrete ordinate method (SHDOM) and takes into account ray tracing, time dependence, Lorentz transformation, elastic Thomson and inelastic Compton scattering. We present numerical test problems with the RRT code.

We describe the method in Section 2 and present test problems in Section 3. The results are summarized in Section 4.

2. METHOD

The RRT code is based on Spherical Harmonic Discrete Ordinate Method (SHDOM, Evans 1998; Pincus & Evans 2009)⁸ code which is a publicly-available static monochromatic radiation transfer code solving the following equation with the Λ iteration (Picard iteration) method.

$$\mathbf{n} \cdot \nabla I_\nu(s, \mathbf{n}) = -\chi_\nu(s, \mathbf{n})I_\nu(s, \mathbf{n}) + \eta_\nu(s, \mathbf{n}), \quad (1)$$

where s is a total path along a ray, \mathbf{n} is direction of travel of the photon, and I_ν , χ_ν , and η_ν are an intensity, an extinction coefficient, and an emission coefficient at frequency ν , respectively. Here, the extinction coefficient is the net absorption coefficient of $\alpha_\nu + \sigma_\nu$, where α_ν and σ_ν are absorption and scattering coefficients, respectively. The SHDOM code is originally developed for radiative transfer in the terrestrial atmosphere and thus correctly treats anisotropic source terms including emission and scattering with spherical harmonics. Equation (1) is integrated for each ray described with discrete ordinates (θ , ϕ) with short characteristic method (ray tracing). The SHDOM code transforms an intensity and a source function between spherical harmonics and discrete ordinates at every time step. The scheme of the SHDOM code, including the transformation between spherical harmonics and discrete ordinates, the ray tracing, and so on, is comprehensively described and validated in Evans (1998) and Pincus & Evans (2009).

In order to apply the SHDOM code to a special relativistic phenomenon, especially a GRB, the following processes and physics are necessary to be included: (1) time dependence because a time step is needed to be

⁷ The production site of photons is much deeper than the scattering photosphere in a relativistic flow (e.g., Shibata et al. 2014).

⁸ <http://nit.colorado.edu/shdom.html>

short enough to capture a relativistic fluid that moves as fast as the light speed, i.e., the light-crossing time is as long as the characteristic dynamical time, (2) Lorentz transformation between laboratory and comoving frames which results in relativistic beaming and a variation of photon frequencies, and (3) anisotropic and inelastic Compton scattering because the photon energy is comparable with the electron rest-mass energy, thus the assumption of Thomson scattering is not valid, and the scattering dominates the opacity in the relativistic jets of GRBs (e.g., Beloborodov 2013).

We set a computational domain to be translationally symmetric along the y axis but the ray of radiation is solved in three dimension and described with polar coordinates θ and ϕ . The coordinates are set to have zenith direction of the z axis and azimuth angle measured from the x axis to the y axis. The radiative transfer equation is solved with the mixed-frame approach (e.g., Mihalas & Mihalas 1984; Hubeny & Burrows 2007); the photon ray is traced in the laboratory frame and the source term is evaluated in the comoving frame. In addition to the above implementation, we update the ray tracing scheme to a cubic Bezier interpolant method (de la Cruz Rodríguez & Piskunov 2013) and include an acceleration scheme of the Λ iteration (Ng acceleration, Ng 1974), but omit the adaptive treatment of mesh points and the parallelization with Message Passing Interface (MPI) for simplicity in this paper.

2.1. Time dependence

A time-dependent radiative transfer equation is written as

$$\frac{1}{c} \frac{\partial I_\nu(t, s, \mathbf{n})}{\partial t} + \mathbf{n} \cdot \nabla I_\nu(t, s, \mathbf{n}) = -\chi_\nu(t, s, \mathbf{n}) I_\nu(t, s, \mathbf{n}) + \eta_\nu(t, s, \mathbf{n}), \quad (2)$$

where c is the light speed. A finite difference approximation to the time derivative is written as

$$\frac{\partial I_\nu(t, s, \mathbf{n})}{\partial t} = \frac{I_\nu(t + \Delta t, s, \mathbf{n}) - I_\nu(t, s, \mathbf{n})}{\Delta t}. \quad (3)$$

The time-dependent radiative transfer equation is deformed to the same shape as the static radiative transfer equation (Eq. 1) with modified absorption and emission coefficients as

$$\mathbf{n} \cdot \nabla I_\nu(t + \Delta t, s, \mathbf{n}) = -\tilde{\chi}_\nu I_\nu(t + \Delta t, s, \mathbf{n}) + \tilde{\eta}_\nu, \quad (4)$$

where

$$\tilde{\chi}_\nu = \chi_\nu(t + \Delta t, s, \mathbf{n}) + \frac{1}{c\Delta t} \quad (5)$$

$$\tilde{\eta}_\nu = \eta_\nu(t + \Delta t, s, \mathbf{n}) + \frac{I_\nu(t, s, \mathbf{n})}{c\Delta t}. \quad (6)$$

Since $I_\nu(t, s, \mathbf{n})$ and Δt are given, the equation (4) can be implicitly solved with the original SHDOM code. Such an implementation of time dependence has been successfully adopted in previous studies (Baron et al. 2009; Hillier & Dessart 2012; Jack et al. 2012). We note that the 4th order Runge-Kutta scheme is adopted to proceed the time step (Appendix A).

2.2. Lorentz transformation

Variables at the next time step are evaluated in the laboratory frame with discrete ordinates with the ray tracing method. The variables are first Lorentz transformed with discrete ordinates to the comoving frame before the conversion from the discrete ordinates to the spherical harmonics. Then, the source terms are evaluated in the comoving frame with spherical harmonics. The source terms are first converted from spherical harmonics to discrete ordinates and then Lorentz transformed from the comoving frame to the laboratory frame. The obtained source term is adopted for the ray tracing in the laboratory frame.

The Lorentz transformation from the laboratory frame to the comoving frame moving with \mathbf{v} , corresponding to the Lorentz factor of Γ , is defined with the following equations (e.g., Mihalas & Mihalas 1984)

$$\nu_0 = \Gamma \nu \left(1 - \frac{\mathbf{n} \cdot \mathbf{v}}{c} \right) \quad (7)$$

$$\mathbf{n}_0 = \frac{\nu}{\nu_0} \left\{ \mathbf{n} - \Gamma \frac{\mathbf{v}}{c} \left[1 - \frac{\Gamma}{\Gamma + 1} \frac{\mathbf{n} \cdot \mathbf{v}}{c} \right] \right\}, \quad (8)$$

where physical values in the comoving frame are denoted with a subscript 0.

The Lorentz transformation is required for an intensity I , an emission coefficient η , and an extinction coefficient χ , whose Lorentz invariants are I/ν^3 , η/ν^2 , and $\chi\nu$, respectively. The frequency and traveling direction of radiation are transformed with Equations (7) and (8).⁹ We prepare (θ, ϕ) mesh points in the laboratory and comoving frames and the Lorentz invariants along the rays, which are transformed from a frame and remapped to the rays in the other frame, and then the intensity, emission coefficient, and absorption coefficient are obtained in the other frame.

2.3. Thomson and Compton scattering

The source function due to scattering is evaluated with spherical harmonics as the original SHDOM code does. Since the prescription is expatiated in Evans (1993, 1998), we briefly describe the procedure. The source function $S(\mu, \phi)$ is expanded in spherical harmonics space as

$$S(\mu, \phi) = \sum_{lm} Y_{lm}(\mu, \phi) S_{lm}, \quad (9)$$

where $Y_{lm}(\mu, \phi)$ are orthonormal real-valued spherical harmonics functions, whereas the phase function of the scattering $\frac{d\sigma}{d\Omega}$ is expanded in a Legendre series in the scattering angle as

$$\frac{d\sigma}{d\Omega} = \sum_{l=0}^{N_L} \chi_l \mathcal{P}_l, \quad (10)$$

where N_L and \mathcal{P}_l are the maximum order of Legendre polynomials, and Legendre polynomials, respectively. The source function is computed as

$$S_{lm} = \frac{\omega \chi_l}{2l + 1} I_{lm} + T_{lm}, \quad (11)$$

⁹ The subroutine is taken from <http://cernlib.web.cern.ch/cernlib/version.html>.

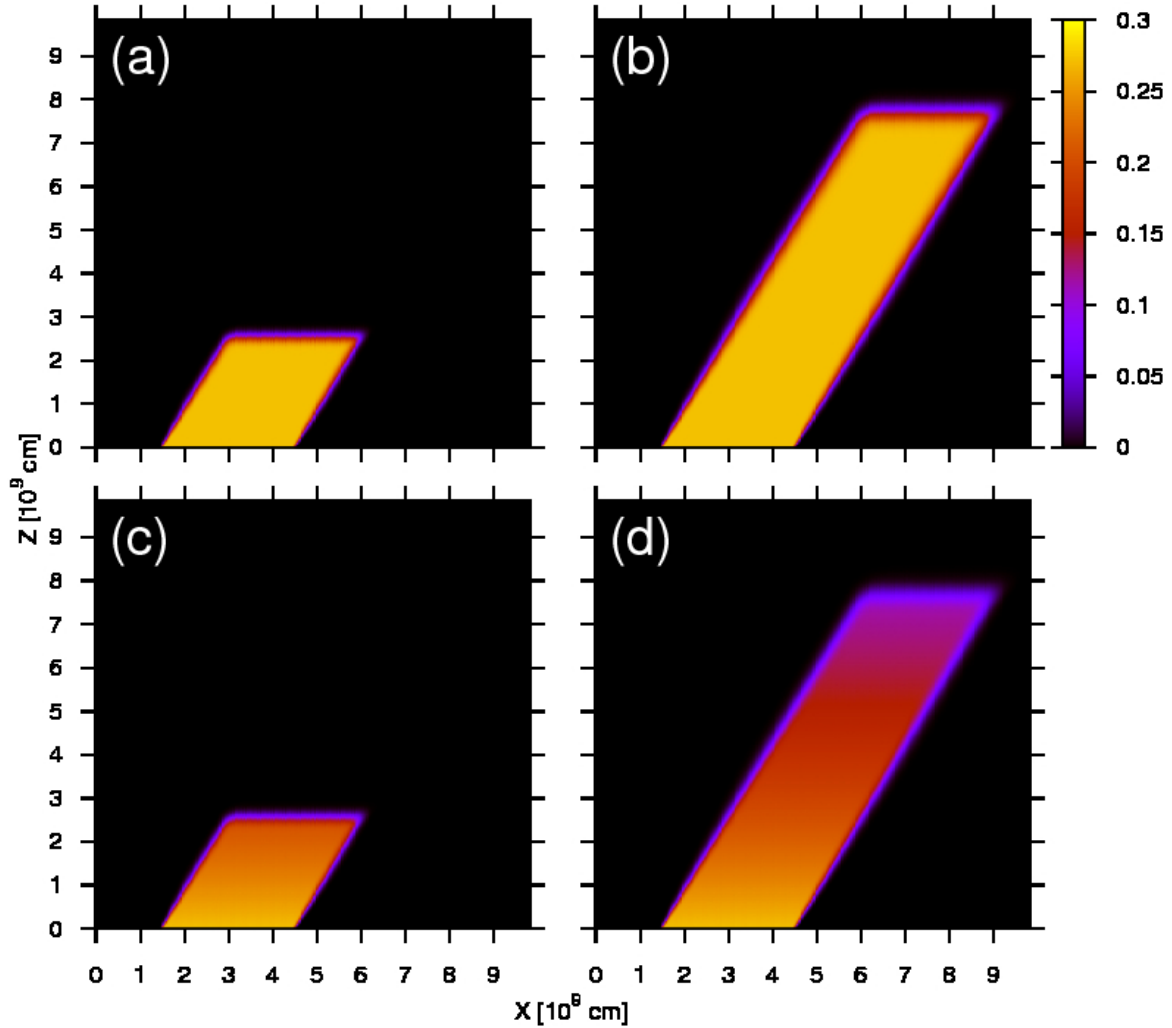


FIG. 1.— Snapshots of mean intensity J for (a) $t = 0.1$ s and $\alpha = 0$, (b) $t = 0.3$ s and $\alpha = 0$, (c) $t = 0.1$ s and $\alpha = 10^{-10}$ cm $^{-1}$, and (d) $t = 0.3$ s and $\alpha = 10^{-10}$ cm $^{-1}$. The medium is at rest ($v = 0$) and the x and z axes are divided by 512 mesh points.

where ω is the single scattering albedo, and I_{lm} and T_{lm} are intensity and thermal emission expanded in spherical harmonics, respectively.

We adopt the phase functions of Thomson and Compton scattering. The phase function of Thomson scattering is

$$\frac{d\sigma_T}{d\Omega} = \frac{r_0^2}{2} (1 + \cos^2 \Theta), \quad (12)$$

where r_0 is the classical electron radius and Θ is the scattering angle (Rybicki & Lightman 1985). Klein-Nishina scattering differential cross section is adopted for the Compton scattering. The equations are

$$\nu_1 = \frac{\nu}{1 + \frac{h\nu}{m_e c^2} (1 - \cos \Theta)} \quad (13)$$

$$\frac{d\sigma}{d\Omega} = \frac{r_0^2}{2} \frac{\nu_1}{\nu} \left(\frac{\nu}{\nu_1} + \frac{\nu_1}{\nu} - \sin^2 \Theta \right), \quad (14)$$

where ν_1 is the photon frequency after the scattering and m_e is the rest mass of electron (Rybicki & Lightman 1985).

A change of the photon frequency and dependence of the scattering kernel on the photon frequency are essential features of the Compton scattering. Therefore, we

implement a multi-group treatment for test calculations of the Compton scattering. The differential cross section $\frac{d\sigma}{d\Omega}|^{(i),(j)}$ of an incident photon in i -th frequency bin with a range of $[\nu^{(i)}, \nu^{(i)} + \Delta\nu^{(i)}]$ to j -th frequency bin with a range of $[\nu_1^{(j)}, \nu_1^{(j)} + \Delta\nu_1^{(j)}]$ is a frequency-dependent scattering kernel defined by Equation (14). $\frac{d\sigma}{d\Omega}|^{(i),(j)}$ is expanded in a Legendre series in the scattering angle with frequency-dependent single scattering albedo. In the mixed-frame approach, the photon exchange between frequency bins takes place only in the comoving frame.

3. TEST PROBLEMS

Evans (1998) and Pincus & Evans (2009) have intensively tested the original SHDOM code and investigated its efficiency, accuracy, and scalability. Therefore, we focus on validation tests of time dependence, Lorentz transformation, and Thomson and Compton scattering in this paper.

3.1. Searchlight beam test

A searchlight beam test has been performed in various studies (e.g., Richling et al. 2001; Turner & Stone 2001; Takahashi et al. 2013; Takahashi & Ohsuga 2013).

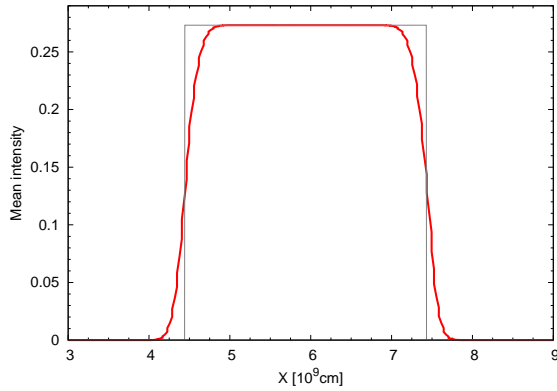


FIG. 2.— Profile section at $z = 5.0 \times 10^9$ cm for the case of $\alpha = 0$ at $t = 0.25$ s (red) and an analytical result (gray).

A narrow beam of light is introduced into the computational domain at a certain angle and the beam crosses the domain. This test examines whether a code can solve a time-dependent radiative transfer equation and how radiation disperses along the path.

We set a computational domain of 10^{10} cm square, of which x and z axes are divided by 512 mesh points. Numbers of angular mesh points are $(N_\theta, N_\phi) = (4, 8)$. The origin is the bottom left corner of the domain. A beam of light is injected from the bottom boundary at 1.5×10^9 cm $< x < 4.5 \times 10^9$ cm along a ray with an angle of $(\theta, \phi) = (0.17\pi, 0)$. Two cases of absorption coefficients are tested; the domain is uniformly filled with a medium with $\alpha = 0$ or $\alpha = 10^{-10}$ cm $^{-1}$.

Figures 1(a)-1(d) show snapshots of the mean intensity J in the domain at $t = 0.1$ s and 0.3 s. The beam crosses the domain properly with time at the injected angle. Figure 2 shows the profile section at $z = 5.0 \times 10^9$ cm and $t = 0.25$ s for the case of $\alpha = 0$. The radiation disperses slightly laterally because the RRT code adopts the short characteristic method.

Figures 3(a)-3(b) show J along $x = \tan(0.17\pi)z + 3.0 \times 10^9$ cm. The figures demonstrate that a wave front proceeds with the light speed. However, the wave front is smeared. This is because the time dependence is taken into account with $\tilde{\chi}$ and $\tilde{\eta}$ which exponentially reduce and/or enhance the intensity as a function of a path length s . The widths of the smooth profile at the wave front are identical for the cases of $\alpha = 0$ and $\alpha = 10^{-10}$ cm $^{-1}$. The mean intensity of the beam is constant for the case of $\alpha = 0$ and is reduced in accordance with $\exp(-\alpha s)$ for the case of $\alpha = 10^{-10}$ cm $^{-1}$. The test confirms that the time dependence and the radiation attenuation are correctly solved by the RRT code although the wave front is smeared.

3.2. Two beam shadow test

A shadow test was proposed in Hayes & Norman (2003). This test examines a reproduction of shadow behind an optically thick blob when plane-parallel radiation illuminates the blob. It is required to properly take into account at least up to the first moment of intensity in order to reproduce the shadow. Thus, for instance, a method with a diffusion approximation fails this test.

On the other hand, a two beam test has been performed in e.g., Davis et al. (2012); Jiang et al. (2012); Sądowski et al. (2013); Jiang et al. (2014). This test ex-

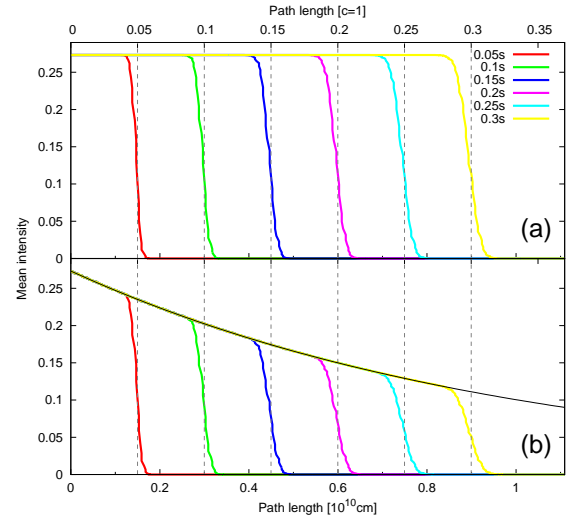


FIG. 3.— Time evolution of the mean intensity J along a ray with $x = \tan(0.17\pi)z + 3.0 \times 10^9$ cm at $t = 0.05$ s (red), 0.1 s (green), 0.15 s (blue), 0.2 s (magenta), 0.25 s (cyan), and 0.3 s (yellow) for the cases of (a) $\alpha = 0$ and (b) $\alpha = 10^{-10}$ cm $^{-1}$. The vertical dashed lines represent analytical expectations of the wave front proceeding with c at $t = 0.05, 0.1, 0.15, 0.2, 0.25$, and 0.3 s (gray dashed). The analytical result of radiation attenuation is also shown (black).

amines whether two independent beams proceeding at different angles pass through without any interactions when they intersect. To describe this phenomenon, it is required to properly take into account at least up to the second moment of intensity. Thus, approximate schemes with a closure relation treating up to the first moment, e.g., the M1 closure method, fail this test.

We solve a two beam with shadow test combining the above tests, which is performed in Davis et al. (2012); Jiang et al. (2012); Sądowski et al. (2013); Jiang et al. (2014). We set an optically thin ($\alpha = 0$) computational domain of 10^{10} cm square, where x and z axes are divided by 512 mesh points. Number of angular mesh points are $(N_\theta, N_\phi) = (4, 8)$. The origin is the bottom left corner of the domain. An optically thick absorptive cylinder with a radius of 1.5×10^9 cm is located at $(x, z) = (5.0 \times 10^9$ cm, 3.3×10^9 cm) perpendicular to the xz plane. The optical depth of the cylinder is set to be $\tau = 100$ with the diameter, i.e., $\alpha = 3.3 \times 10^{-8}$ cm $^{-1}$. Plane-parallel radiation is injected from the bottom boundary at angles of $(\theta, \phi) = (0.17\pi, 0)$ and $(0.17\pi, \pi)$.

Figures 4a-4b show snapshots of J in the domain at $t = 0.2$ and 1.0 s. The plane-parallel radiation proceeds properly with time and the wave speed is the speed of light. A shadow develops behind the cylinder along the directions of two beams and the two beams cross around $(x, z) = (5.0 \times 10^9$ cm, 7.4×10^9 cm) without any interaction. The test confirms that the calculation properly solves the radiation transfer equation for intensity.

3.3. Radiative pulse test

The RRT code is tested with the evolution of a radiative pulse initially having a Gaussian profile in an optically thin medium and a scattering-dominated optically thick medium. The tests have been performed in Sądowski et al. (2013) and verify the treatments of time dependence and scattering.

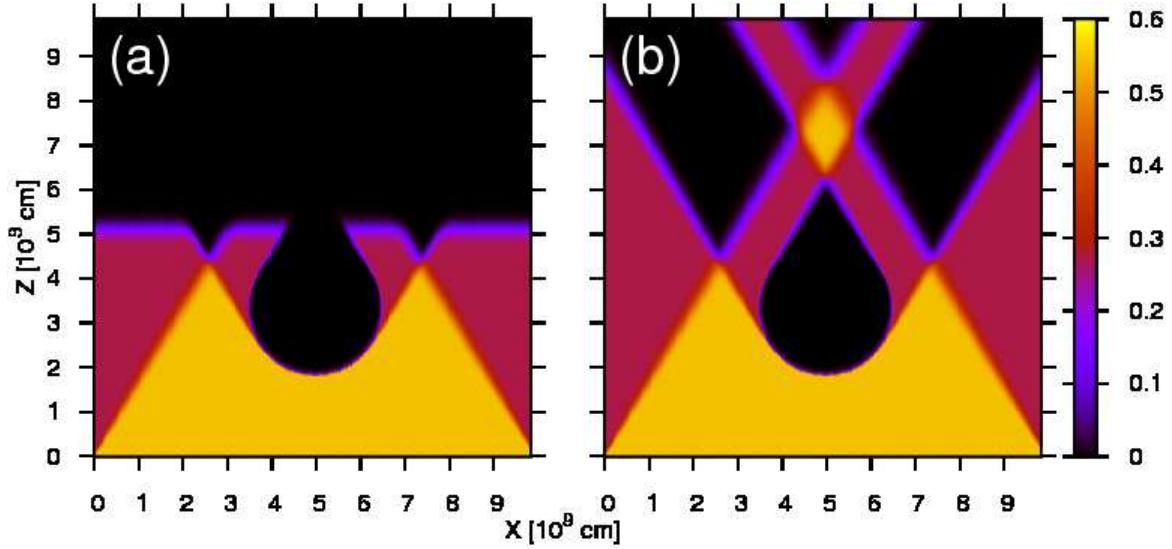


FIG. 4.— Snapshots of the mean intensity J for the two beam and shadow test at (a) $t = 0.2$ s and (b) 1.0 s. The light is injected from the bottom boundary at the angles with $(\theta, \phi) = (0.17\pi, 0)$ and $(0.17\pi, \pi)$. An optically thick cylinder with $\alpha = 3.3 \times 10^{-8} \text{ cm}^{-1}$ and a radius of $1.5 \times 10^9 \text{ cm}$ is located at $(x, z) = (5.0 \times 10^9 \text{ cm}, 3.3 \times 10^9 \text{ cm})$. The medium is at rest ($v = 0$) and the x and z axes are divided by 512 mesh points.

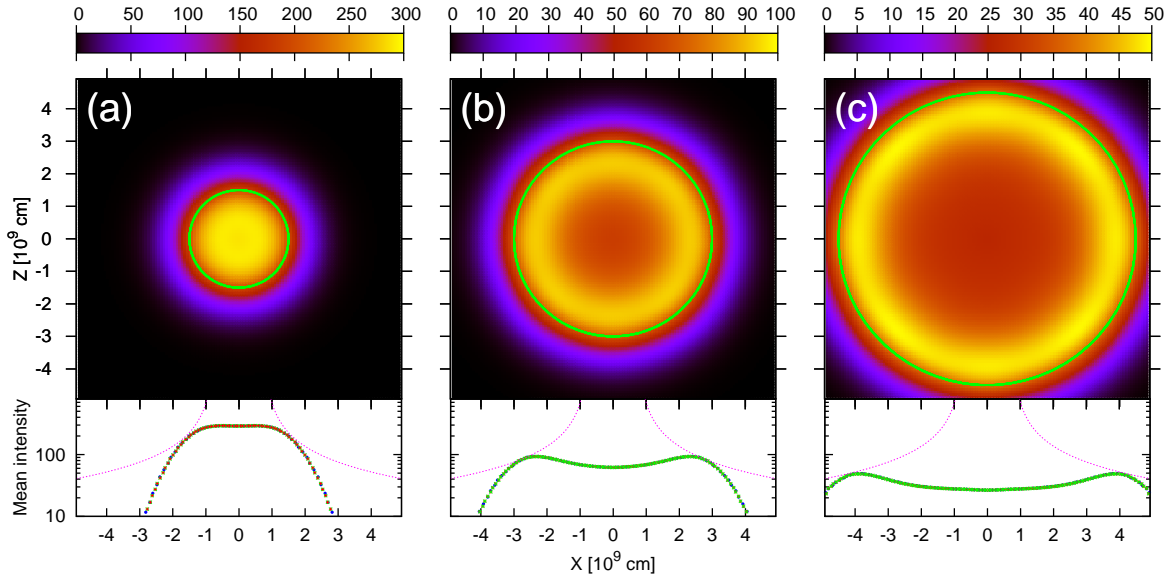


FIG. 5.— (Top) Snapshots of the mean intensity J for the optically thin ($\chi = 0$) radiative pulse test at $t = 0.1$ s (left), 0.2 s (middle), and 0.3 s (right). (Bottom) Profile section of the mean intensity along the x axis (red), z axis (green), and $x = z$ (blue) at $t = 0.1$ s (left), 0.2 s (middle), and 0.3 s (right). The $1/r$ dependence is also shown in the bottom panels (magenta).

3.3.1. Optically thin medium

In the optically thin limit, the isotropic radiative pulse spreads with the speed of light and the mean intensity decreases inversely proportionally to the radius in the translational symmetry.

We set an optically thin computational domain of 10^{10} cm square with $\alpha = 0$. The origin is at the center of the domain. Each axis is divided by 128 mesh points. Number of angular mesh points are $(N_\theta, N_\phi) = (64, 128)$. An initial radiative pulse is set according to the equation

$$I_0(\mathbf{x}, \mathbf{n}) = 100 \exp \left[- \left(\frac{r}{w} \right)^2 \right], \quad (15)$$

where r ($= |\mathbf{x}|$) is the distance from the origin and $w = 9.0 \times 10^8 \text{ cm}$. The intensity of the pulse is initially

isotropic at each mesh point.

The top panels of Figure 5 show snapshots of J at $t = 0.1$ s, 0.2 s, and 0.3 s. The expected size of the pulse is also shown by a green circle with a radius of ct . The bottom panels of Figure 5 show J along x axis, z axis, and a line with $x = z$ at $t = 0.1$ s, 0.2 s, and 0.3 s. These profiles of J are identical and the peak of J decreases with the expansion of the pulse according to $J \propto 1/r$ as expected. The result demonstrates that the pulse isotropically propagates with the speed of light and that the geometrical dilution of radiation is correctly followed with the RRT code.

3.3.2. Optically thick medium

In the scattering-dominated optically thick medium, the radiative pulse diffuses out. A one-dimensional dif-

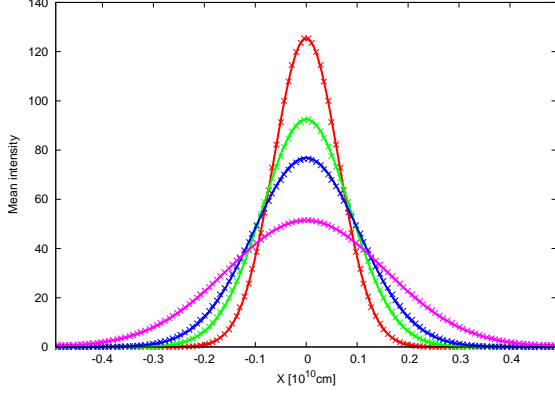


FIG. 6.— Profile section of the mean intensity J along the x axis (crosses) for the optically thick ($\sigma = 3 \times 10^{-8} \text{ cm}^{-1}$) radiative pulse test at $t = 0$ (red), 0.5 s (green), 1.0 s (blue), and 3.0 s (magenta). The solid lines show the exact solution (Eq. 16).

fusion equation $\frac{\partial J}{\partial t} = \chi \frac{\partial^2 J}{\partial x^2}$ can be solved analytically and the solution is written as

$$J(t, x) = \frac{1}{2\sqrt{\chi\pi t}} \int_{-\infty}^{\infty} J_0(x') \exp \left\{ -\frac{(x-x')^2}{4\chi t} \right\} dx' \quad (16)$$

where $\chi = \frac{1}{3c\sigma}$ and $J_0(x)$ is the initial profile of the radiative pulse.

We set the optically thick computational domain of 10^{10} cm square with $\tau = 300$ along a side, i.e., $\sigma = 3 \times 10^{-8} \text{ cm}^{-1}$. The origin is set at the center of the domain. Each axis is divided by 128 mesh points. Number of angular mesh points are $(N_\theta, N_\phi) = (32, 64)$. The each mesh point is optically thick, $\tau = 2.3$, so that most of the photons are scattered at least once in the mesh point. Here, we adopt a spherical scattering kernel. A radiative pulse is initially set according to

$$I_0(\mathbf{x}, \mathbf{n}) = 100 \exp \left[-\left(\frac{x}{w} \right)^2 \right] \quad (17)$$

where $w = 9.0 \times 10^8 \text{ cm}$. The intensity of the pulse is initially isotropic at each mesh point.

Figure 6 shows the time evolution of J along the x axis. The radiation gradually diffuses in the numerical simulation and the distribution of J well reproduces that of the analytic solution at every time step until the radiation reaches the boundaries of the computational domain.

3.4. Relativistic beaming test

We validate the ability of the RRT code to treat the relativistic beaming as a result of the Lorentz transformation. This is a characteristic feature of a special relativistic radiative transfer calculation. Although the propagation of beam of light along a curved trajectory is demonstrated in general relativistic radiative transfer calculations (e.g., Sądowski et al. 2013), this is the first attempt to confirm the relativistic beaming in special relativistic calculations.

We set a computational domain of 10^{10} cm square filled with the optically thin medium with $\alpha = 0$ and consider a cylindrical light source with a radius of $R = 5 \times 10^8 \text{ cm}$ at the center of a computational domain. The center of a computational domain is set to be the origin. In the cylinder, particles move with $\mathbf{v} = (v_x, v_z)$ with respect to the laboratory frame and emit photons isotropically in

the comoving frame of each particle, whereas they do not emit any photons and not interact with photons outside the cylinder. Each axis is divided by 128 mesh points and number of angular mesh points are $(N_\theta, N_\phi) = (32, 64)$.

Figures 7a-7f show snapshots of the normalized mean intensity J/J_{max} in the Laboratory frame at $t = 0.2 \text{ s}$ for the cases with $(v_x, v_z) = (0, 0)$, $(0.1c, 0)$, $(0.5c, 0)$, $(0.9c, 0)$, $(0.99c, 0)$, and $(0.995c, 0)$, respectively, where J_{max} is the maximum mean intensity in the computational domain. The corresponding Lorentz factors are $\Gamma = 1, 1.005, 1.15, 2.29, 7.09$, and 10.0 . It is clearly shown that the mean intensity is high along the direction of \mathbf{v} . An analytic expression of the beaming effect (asymptotically $\theta \sim \frac{1}{\Gamma}$, Rybicki & Lightman 1985) is also shown with green lines circumscribing the light source. The biased distribution of J in the calculation is consistent with the analytic expression. The test shows that the beaming effect is correctly taken into account in the RRT code.

The speed of $0.995c$ is close to the maximum speed that can be correctly solved with $N_\theta = 32$ because the half-angle of the concentration of radiation for the case of $v = 0.9952c$ is comparable to the interval between angular mesh points. Although the test is limited due to computational resources, the Lorentz factor as high as the one encountered in GRB models can be resolved by the RRT code, if the larger number of angular mesh points is adopted, because the mapping subroutine for the Lorentz transformation is valid even for high Lorentz factor. Figure 8 shows the angular distribution of the intensity I in the laboratory frame for the cases with $(v_x, c-v_z) = (0, 5 \times 10^{-3}c)$ ($\Gamma = 10$), $(0, 5 \times 10^{-5}c)$ ($\Gamma = 100$), $(0, 6 \times 10^{-6}c)$ ($\Gamma = 300$), and $(0, 5 \times 10^{-7}c)$ ($\Gamma = 1000$), which is transformed from an isotropic intensity I_0 in the comoving frame. The deviation from the analytical solution $I(\mu) = (\Gamma(1 - \mu v_z/c))^{-3} I_0$ is less than $10^{-6} I$. Here, we adopt the large number of angular mesh points of $(N_\theta, N_\phi) = (4096, 8192)$. We note that the mapping subroutine correctly transforms an isotropic radiation for any Lorentz factor even with the small number of angular mesh points.

3.5. Comparison with Monte Carlo method

The original SHDOM code and the Monte Carlo method have been carefully compared and their drawback and advantage have been presented in Evans (1998) and Pincus & Evans (2009). Therefore, we test the RRT code only on the treatments of the Thomson and Compton scattering and Lorentz transformation, and the implementation of multiple frequency groups for the Compton scattering tests, by comparing solutions of a shadow test of the RRT code with those of a relativistic Monte Carlo (RMC) code (S. Shibata & N. Tominaga in prep., Appendix B for a test of the RMC code). In this subsection, we omit the time dependence and adopt the static version of the RRT code because the RMC code currently does not follow the time evolution of the radiation.

Here, we adopt an ideal test problem. A scattering-dominated optically thick cylinder with $\sigma = \sigma_0 \exp \left(-\frac{r^2}{w^2} \right)$, where $\sigma_0 = 2 \times 10^{-7} \text{ cm}^{-1}$ and $w = 2.5 \times 10^8 \text{ cm}$, is put at the center of the optically thin computational domain of 10^{10} cm square with $\sigma = 2 \times 10^{-15} \text{ cm}^{-1}$. Scattering particles rest or flow with \mathbf{v} in the scatter-

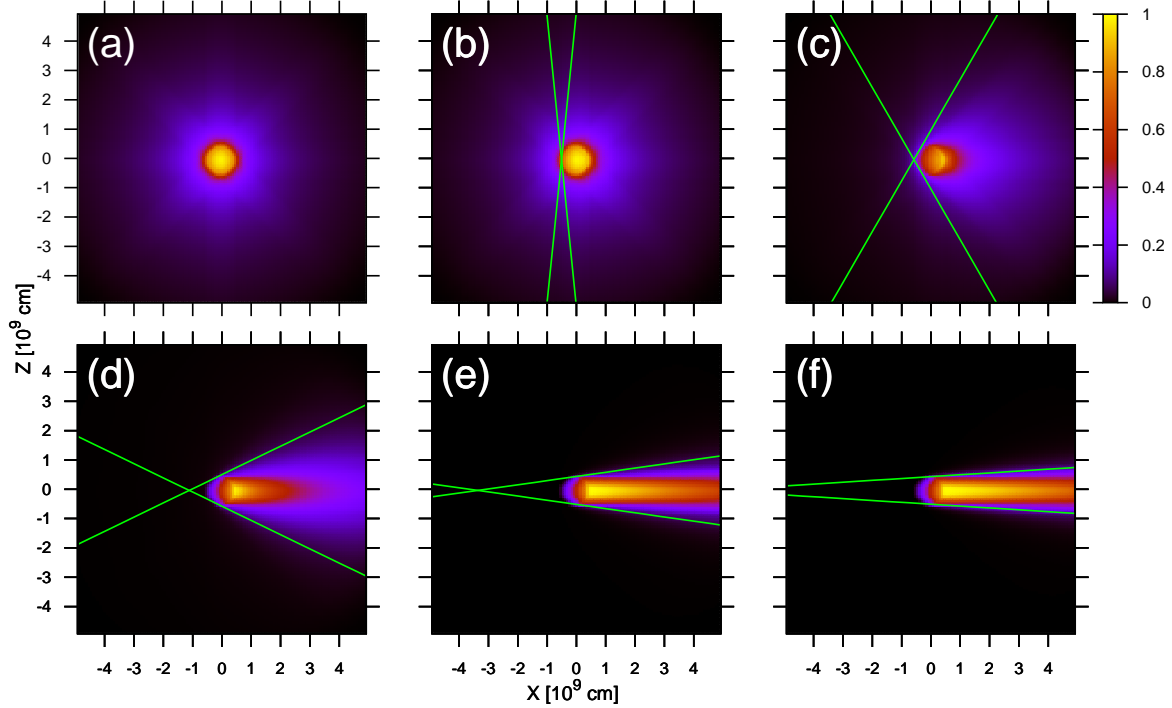


FIG. 7.— Snapshots of the mean intensity normalized with the maximum mean intensity J/J_{\max} for the relativistic beaming test for the cases of (a) $(v_x, v_z) = (0, 0)$, (b) $(v_x, v_z) = (0.1c, 0)$, (c) $(v_x, v_z) = (0.5c, 0)$, (d) $(v_x, v_z) = (0.9c, 0)$, (e) $(v_x, v_z) = (0.99c, 0)$, and (f) $(v_x, v_z) = (0.995c, 0)$. Asymptotic analytic expressions of the beaming effect are also shown (green lines).

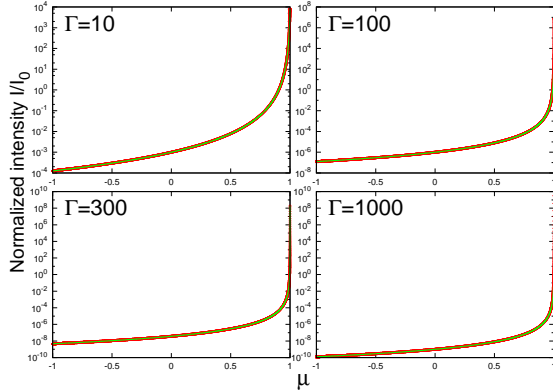


FIG. 8.— Distribution of the normalized intensity I/I_0 as a function of the zenith angle for the numerical solution (red) and the analytic solution (green).

ing cylinder.¹⁰ Plane-parallel radiation is injected from the left and bottom boundaries at a single angle of $(\theta, \phi) = (0.24\pi, 0)$. The incident angle of radiation is set to the same in the RRT and RMC calculations.

3.5.1. Thomson scattering

In this subsection, we adopt a kernel of Thomson scattering. The computational domain is divided by 128×128 mesh points and numbers of angular mesh points are $(N_\theta, N_\phi) = (160, 320)$.

Figures 9(a)-9(b), and 9(c)-9(d) show normalized z -oriented fluxes $F_z(x, z)/F_{z, \max}$ obtained by the RRT and RMC calculations in the cases with $(v_x, v_z) = (0, 0)$ and

¹⁰ We assume, for example, an ideal atom that do not interact with the photons if they are neutral and that the atoms rest or flow with \mathbf{v} in the computational domain and its ionization fraction changes to reproduce the distribution of σ .

$(0, 0.9c)$, respectively, where $F_{z, \max}$ is the maximum z -oriented flux in the computational domain. Figures 9(a)-9(b) demonstrate that the z -oriented fluxes are small below the cylinder due to the scattered photons propagating to the $-z$ direction, whereas the z -oriented fluxes are high at the top left side of the cylinder. Since the number density of scattered photons decreases with the distance from the scattering cylinder as $1/r$, the z -oriented fluxes are prominently modified around the cylinder. Also the shadow behind the cylinder consistently forms in both calculations. Figures 9(c)-9(d) shows that the scattered photons are concentrated to the $+z$ direction due to the relativistic beaming in both calculations. These demonstrate that the RRT code well solves the anisotropic scattering and the Lorentz transformation.

3.5.2. Compton scattering

In this subsection, we adopt frequency-dependent kernels of Compton scattering and the multi-group treatment. The computational domain is divided by 64×64 mesh points. We test the RRT code for 2 cases with different velocity of scattering particles with $(v_x, v_z) = (0, 0)$ and $(0, 0.9c)$. Numbers of angular mesh points are $(N_\theta, N_\phi) = (128, 256)$. The frequency range is equally divided by 10 bins in both cases but the maximum frequency is $h\nu = 1.1m_e c^2$ for the cases with $(v_x, v_z) = (0, 0)$ and $4.0m_e c^2$ for the case with $(v_x, v_z) = (0, 0.9c)$. Monochromatic light with $h\nu = 1.05m_e c^2$ for the cases with $(v_x, v_z) = (0, 0)$ and $h\nu = 1.0m_e c^2$ for the case with $(v_x, v_z) = (0, 0.9c)$ is injected.

Figures 10(a)-10(f) and 11(a)-11(f) show frequency-dependent normalized z -oriented fluxes $F_{\nu, z}(x, z)/F_{\nu, z, \max}$ in the cases with $(v_x, v_z) = (0, 0)$ and $(0, 0.9c)$, respectively, where $F_{\nu, z, \max}$ is the maximum z -oriented flux in a frequency bin in the computational

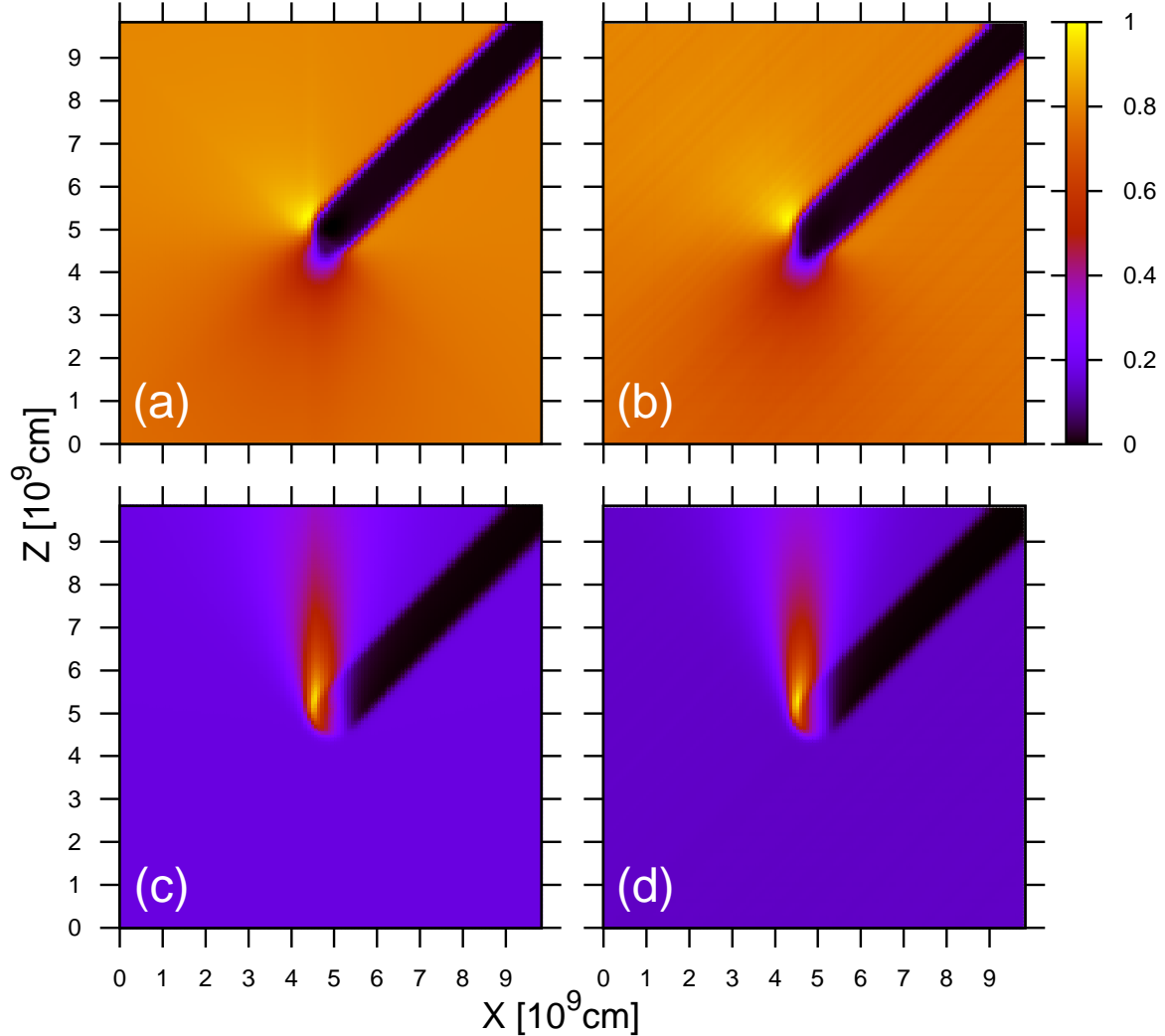


FIG. 9.— Snapshots of z -oriented fluxes normalized with the maximum flux $F_z(x, z)/F_{z, \max}$ in the medium with $(v_x, v_z) = (0, 0)$ [(a) and (b)] and $(v_x, v_z) = (0, 0.9c)$ [(c) and (d)]. The panels show the results of the RRT code [(a) and (c)] and the RMC code [(b) and (d)]. Here, the Thomson scattering kernel is adopted and the plane-parallel radiation is injected from the left and bottom boundaries at a single angle of $(\theta, \phi) = (0.24\pi, 0)$.

domain. Each panel shows the fluxes in different energy bins. There was no light in these energy bins before scattering. This is the reason why no shadow appears behind the cylinder. The negative fluxes due to the scattered photons produce the black region below the cylinder in Figure 10(e) and 10(f). Although the shape of $F_{\nu, z}(x, z)$ is smeared in the RRT code, especially in the case of $(v_x, v_z) = (0, 0.9c)$, because the frequency of photons is converted to the central frequency of each bin at every time step, it provides the similar snapshots of the z -oriented flux in the RMC code. These display that the RRT code correctly solves the Compton scattering and the Lorentz transformation, and well treats the multi-group radiation transfer equation.

4. SUMMARY

We develop a time-dependent multi-group multidimensional relativistic radiative transfer code by implementing the treatments of time dependence, multi-frequency bins, Lorentz transformation, and elastic Thomson and inelastic Compton scattering to the publicly available SHDOM code. The SHDOM code evaluates a source

function in spherical harmonics and solves a static radiative transfer equation with a ray tracing in discrete ordinates. The RRT code is validated by the various tests and the comparison with the RMC calculations. The searchlight beam, two beam with shadow, radiative pulse, and relativistic beaming tests are successfully passed by the RRT code and confirm that the RRT code correctly handles the time dependence and the Lorentz transformation. The results of the RRT code are consistent with those of the RMC code and the comparisons verify the implementation of elastic Thomson and inelastic Compton scattering and multi-group treatment in the RRT code. The RMC code, in turn, is validated against the EGS tools (Appendix B).

The RRT code enables us to obtain the evolution of intensity and thus to self-consistently derive an Eddington tensors without approximations like the flux limited diffusion or the M1 closure methods. We emphasize that the radiation tends to be more anisotropic in the relativistic fluid because of the Lorentz transformation and Compton scattering for the γ -ray photons, and thus that the angular distribution of radiation should

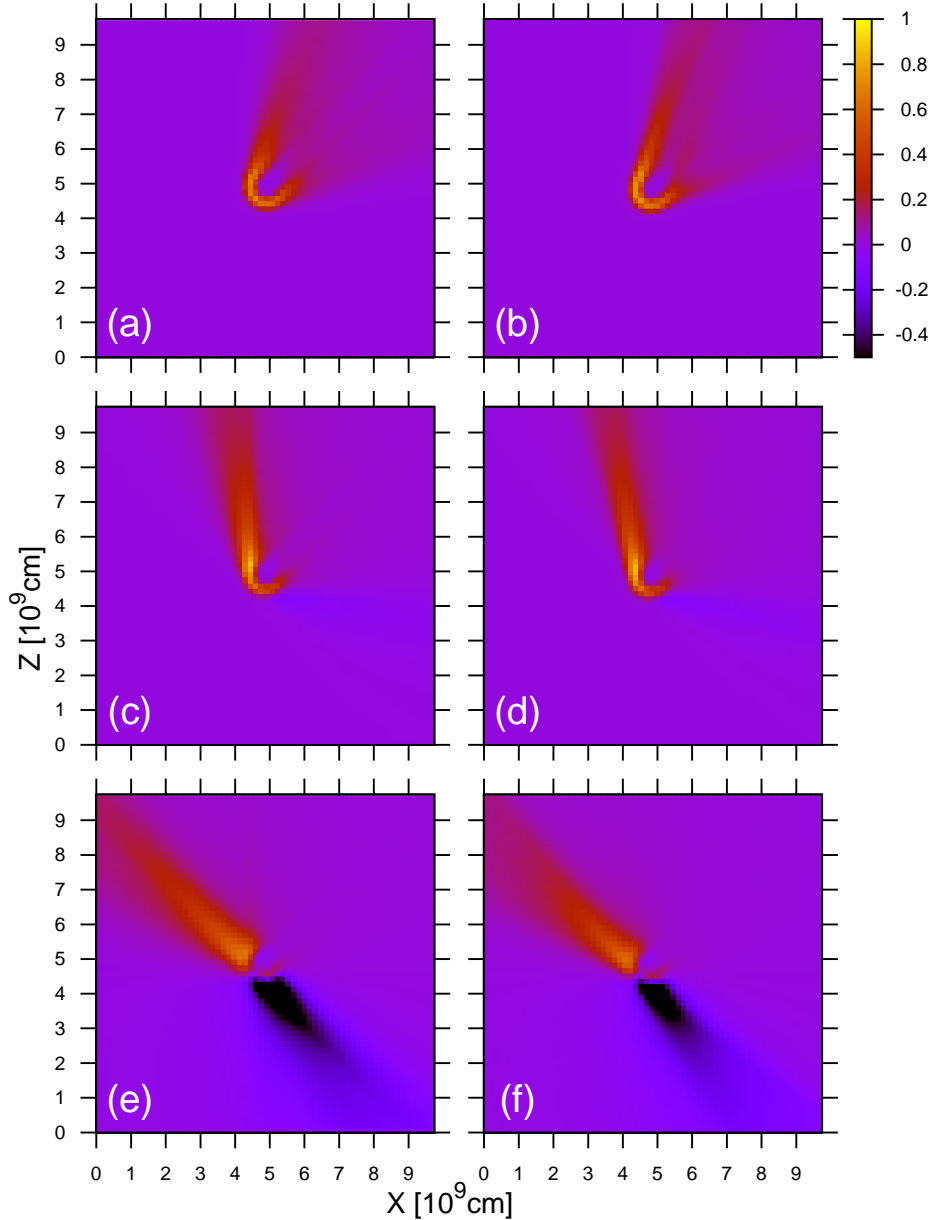


FIG. 10.— Snapshots of frequency-dependent z -oriented fluxes normalized with the maximum flux $F_{\nu,z}(x,z)/F_{\nu,z,\max}$ in the cases with $(v_x, v_z) = (0, 0)$. The panels represent fluxes at the energy bins with $[0.88m_e c^2, 0.99m_e c^2]$ [(a) and (b)], $[0.66m_e c^2, 0.77m_e c^2]$ [(c) and (d)], and $[0.44m_e c^2, 0.55m_e c^2]$ [(e) and (f)]. The panels show the results of the RRT code [(a), (c), and (e)] and the RMC code [(b), (d), and (f)]. Here, the frequency-dependent Compton scattering kernels are adopted.

be properly taken into account. Combining the Eddington tensors with relativistic hydrodynamics calculations (e.g., Tominaga 2009), a relativistic radiation hydrodynamics will be realized with the variable Eddington tensor method. Furthermore, the RRT code implicitly solves the radiative transfer equation and thus can follow the radiative transfer in a non-relativistic fluid like a supernova without adopting unnecessarily short time steps. Such a method will be useful to clarify the connection between GRBs and supernovae.

It is currently difficult to increase the numbers of frequency bins, and angular and spatial mesh points due to an available memory resource. The difficulties are solved if the adaptive treatment of mesh points and the parallelization with distributed memory are implemented be-

cause the ray tracing in the laboratory frame and the evaluation of source function in the comoving frame are independent of each ray and each mesh point, respectively. However, we note the low resolution of the frequency is an intrinsic drawback of the multi-group treatment compared to the Monte Carlo method, in which a frequency of each photon changes continuously. Thus, the Monte Carlo method is superior to the RRT code for spectral synthesis calculations of lines and fine spectral features. However, the method intrinsically involves a noise and it is expensive to reduce the noise because the reduction is realized only proportional to the square root of the number of photon packets.¹¹ And, the large

¹¹ Several techniques are suggested to reduce the noise (e.g., Steinacker et al. 2013; Roth & Kasen 2015).

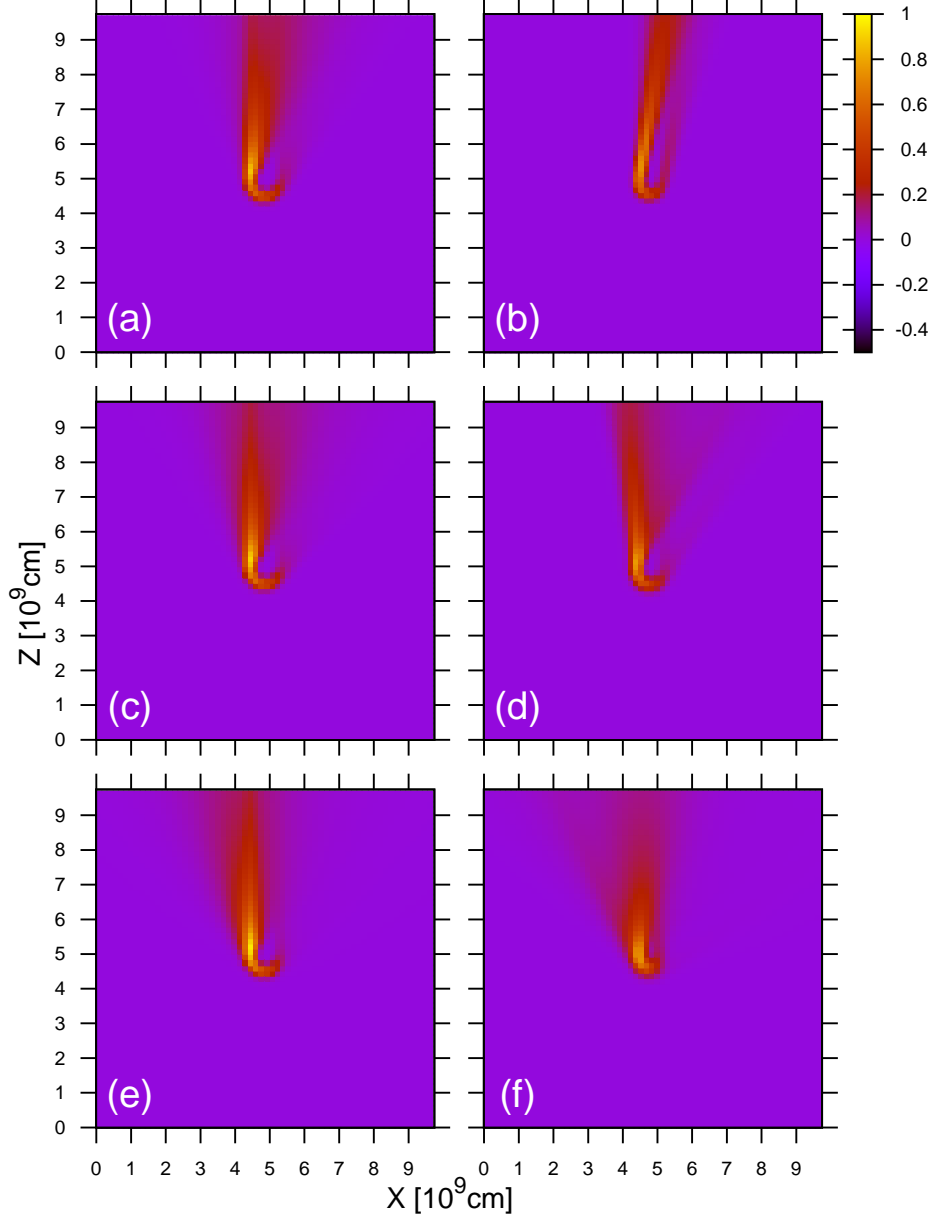


FIG. 11.— Same as Figure 10 but for the cases with $(v_x, v_z) = (0, 0.9c)$. The panels represent fluxes at the energy bins with $[2.0m_e c^2, 2.4m_e c^2]$ [(a) and (b)], $[1.2m_e c^2, 1.6m_e c^2]$ [(c) and (d)], and $[0.4m_e c^2, 0.8m_e c^2]$ [(e) and (f)].

number of photon packets is necessary to follow the time dependence because the photon packets are emitted at each time step. Furthermore, the radiation contributes to the hydrodynamics with an integration of radiation over all frequency and the dynamical effects of the radiation in GRBs are not dominated by narrow spectral lines. Thus, we propose a post-processing Monte Carlo calculation for spectral synthesis after a time-dependent matter-coupled relativistic radiative transfer calculation.

N.T. thanks Hajime Susa for fruitful discussion. This research has been supported in part by the RFBR-JSPS bilateral program, World Premier International Research Center Initiative, MEXT, Japan, and by the Grants-in-Aid for Scientific Research of the JSPS (23740157, 15H05440). S.B. is supported by the Russian Science Foundation Grant No. 14-12-00203. Calculations were in part carried out on the general-purpose PC farm at Center for Computational Astrophysics, National Astronomical Observatory of Japan.

APPENDIX

TIME INTEGRATION

We treat the time dependence with the modified absorption and emission coefficients as shown in Section 2.1, and implicitly obtain the self-consistent time-dependent intensity at $t + \Delta t$. Although the time derivative is differentiated in the first order, we adopt the 4th order Runge-Kutta scheme to proceed the time step from t to $t + \Delta t$ by dividing the time interval to 4 steps, in order to increase the accuracy by adopting smaller time intervals.

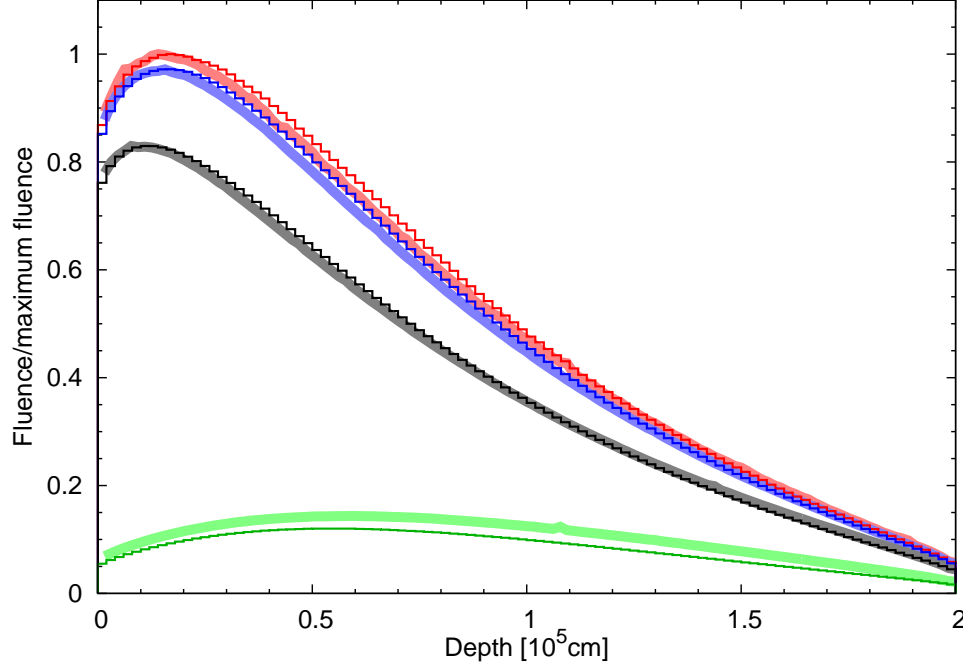


FIG. 12.— Fluence as a function of the depth calculated with the RMC code (thick) and the EGS tool (thin). The color represents the rings with $r < 1 \times 10^4$ cm (red), 1×10^4 cm $< r < 5 \times 10^4$ cm (blue), 5×10^4 cm $< r < 1 \times 10^5$ cm (black), and 1×10^5 cm $< r < 2 \times 10^5$ cm (green).

$$I_\nu(t + \Delta t, s, \mathbf{n}) = I_\nu(t, s, \mathbf{n}) + \Delta I_\nu^{(1)} + \Delta I_\nu^{(2)} + \Delta I_\nu^{(3)} + \Delta I_\nu^{(4)}, \quad (\text{A1})$$

where

$$\Delta I_\nu^{(1)} = \mathcal{J}_\nu(\Delta t/6, I_\nu(t, s, \mathbf{n})) - I_\nu(t, s, \mathbf{n}) \quad (\text{A2})$$

$$I_\nu^{(1)} = I_\nu(t, s, \mathbf{n}) + 3\Delta I_\nu^{(1)} \quad (\text{A3})$$

$$\Delta I_\nu^{(2)} = \mathcal{J}_\nu(\Delta t/3, I_\nu^{(1)}) - I_\nu^{(1)} \quad (\text{A4})$$

$$I_\nu^{(2)} = I_\nu(t, s, \mathbf{n}) + \frac{3}{2}\Delta I_\nu^{(2)} \quad (\text{A5})$$

$$\Delta I_\nu^{(3)} = \mathcal{J}_\nu(\Delta t/3, I_\nu^{(2)}) - I_\nu^{(2)} \quad (\text{A6})$$

$$I_\nu^{(3)} = I_\nu(t, s, \mathbf{n}) + 3\Delta I_\nu^{(3)} \quad (\text{A7})$$

$$\Delta I_\nu^{(4)} = \mathcal{J}_\nu(\Delta t/6, I_\nu^{(3)}) - I_\nu^{(3)}. \quad (\text{A8})$$

Here, $\mathcal{J}_\nu(\Delta t, I_\nu)$ is the solution of Equation (4) with I_ν and Δt , i.e., $\mathcal{J}_\nu(\Delta t, I_\nu(t, s, \mathbf{n})) = I_\nu(t + \Delta t, s, \mathbf{n})$.

COMPARISON WITH ELECTRON GAMMA SHOWER (EGS) SOFTWARE

We compare the result of the RMC code with that of National Research Council's electron gamma shower (EGS) software tool¹² to confirm its validity, especially the treatment of the scattering. EGS software is a publicly available code that enables sophisticated treatment of photon, electron, and positron transfer in complicated medium and provides graphic tools to show numerical results. Here, we adopt *flurznrc* package only with the Compton scattering by electrons at rest in the EGS software.

We set a cylindrical computational domain with a radius of 2×10^5 cm and a depth of 2×10^5 cm. The cylinder is filled with H atoms with a number density of 8.37×10^{-5} g cm⁻³. The incident photons with 50 keV are vertically injected from the top boundary with $r < 1 \times 10^5$ cm, where r is the distance from the center of the top boundary.

Figure 12 shows a comparison with the fluence as a function of the depth in rings with $r < 1 \times 10^4$ cm, 1×10^4 cm $< r < 5 \times 10^4$ cm, 5×10^4 cm $< r < 1 \times 10^5$ cm, and 1×10^5 cm $< r < 2 \times 10^5$ cm, normalized by the maximum fluence. The fluence is defined as a summation of $1/|\cos\theta|$ for all photons per unit area at each boundary of slabs, where θ is the angle the photon makes with respect to the normal to the plane. We adopt 6×10^7 photons for both of the RMC calculation and the calculation by the EGS tool. The RMC codes give consistent results with that obtained by the

¹² http://www.nrc-cnrc.gc.ca/eng/solutions/advisory/egsnrc_index.html

EGS software.

REFERENCES

- Abdo, A. A. et al. 2009a, *ApJ*, 706, L138
 ——. 2009b, *Science*, 323, 1688
 Amati, L. et al. 2002, *A&A*, 390, 81
 Amati, L., Guidorzi, C., Frontera, F., Della Valle, M., Finelli, F., Landi, R., & Montanari, E. 2008, *MNRAS*, 391, 577
 Asplund, M., Nordlund, Å., Trampedach, R., Allende Prieto, C., & Stein, R. F. 2000, *A&A*, 359, 729
 Baron, E., Hauschildt, P. H., & Chen, B. 2009, *A&A*, 498, 987
 Beloborodov, A. M. 2011, *ApJ*, 737, 68
 ——. 2013, *ApJ*, 764, 157
 Blinnikov, S. I., Kozyreva, A. V., & Panchenko, I. E. 1999, *Astronomy Reports*, 43, 739
 Clough, S. A., Shephard, M. W., Mlawer, E. J., Delamere, J. S., Iacono, M. J., Cady-Pereira, K., Boukabara, S., & Brown, P. D. 2005, *J. Quant. Spec. Radiat. Transf.*, 91, 233
 Collins, W. D. et al. 2006, *Journal of Geophysical Research (Atmospheres)*, 111, 14317
 Cucchiara, A. et al. 2011, *ApJ*, 736, 7
 Dainotti, M. G., Cardone, V. F., & Capozziello, S. 2008, *MNRAS*, 391, L79
 Davis, S. W., Stone, J. M., & Jiang, Y.-F. 2012, *ApJS*, 199, 9
 de la Cruz Rodríguez, J., & Piskunov, N. 2013, *ApJ*, 764, 33
 Dexter, J., & Agol, E. 2009, *ApJ*, 696, 1616
 Evans, K. F. 1993, *Journal of Atmospheric Sciences*, 50, 3111
 ——. 1998, *Journal of Atmospheric Sciences*, 55, 429
 Fan, Y.-Z. et al. 2013, *ApJ*, 776, 95
 Giannios, D. 2006, *A&A*, 457, 763
 Gorbovskoy, E. S. et al. 2012, *MNRAS*, 421, 1874
 Hayes, J. C., & Norman, M. L. 2003, *ApJS*, 147, 197
 Hillier, D. J., & Dessart, L. 2012, *MNRAS*, 424, 252
 Hubeny, I., & Burrows, A. 2007, *ApJ*, 659, 1458
 Iliev, I. T. et al. 2006, *MNRAS*, 371, 1057
 ——. 2009, *MNRAS*, 400, 1283
 Ito, H. et al. 2013, *ApJ*, 777, 62
 Jack, D., Hauschildt, P. H., & Baron, E. 2012, *A&A*, 546, A39
 Jiang, Y.-F., Stone, J. M., & Davis, S. W. 2012, *ApJS*, 199, 14
 ——. 2014, *ApJS*, 213, 7
 Krumholz, M. R., Klein, R. I., & McKee, C. F. 2007, *ApJ*, 656, 959
 Lazzati, D., Morsony, B. J., Margutti, R., & Begelman, M. C. 2013, *ApJ*, 765, 103
 Levan, A. J. et al. 2014, *ApJ*, 781, 13
 Lundman, C., Pe'er, A., & Ryde, F. 2013, *MNRAS*, 428, 2430
 Mészáros, P. 2006, *Reports on Progress in Physics*, 69, 2259
 Mihalas, D., & Mihalas, B. W. 1984, *Foundations of radiation hydrodynamics*
 Mizuta, A., Nagataki, S., & Aoi, J. 2011, *ApJ*, 732, 26
 Nagakura, H., Ito, H., Kiuchi, K., & Yamada, S. 2011, *ApJ*, 731, 80
 Nagakura, H., Sumiyoshi, K., & Yamada, S. 2014, *ApJS*, 214, 16
 Ng, K.-C. 1974, *J. Chem. Phys.*, 61, 2680
 Nordlund, Å., Stein, R. F., & Asplund, M. 2009, *Living Reviews in Solar Physics*, 6, 2
 Pe'er, A. 2008, *ApJ*, 682, 463
 Pincus, R., & Evans, K. F. 2009, *Journal of Atmospheric Sciences*, 66, 3131
 Richling, S., Meinköhn, E., Kryzhevov, N., & Kanschat, G. 2001, *A&A*, 380, 776
 Roth, N., & Kasen, D. 2015, *ApJS*, 217, 9
 Rybicki, G. B., & Lightman, A. P. 1985, *Radiative processes in astrophysics*.
 Ryde, F. et al. 2010, *ApJ*, 709, L172
 Salvaterra, R. et al. 2009, *Nature*, 461, 1258
 Sądowski, A., Narayan, R., Tchekhovskoy, A., & Zhu, Y. 2013, *MNRAS*, 429, 3533
 Shcherbakov, R. V., & Huang, L. 2011, *MNRAS*, 410, 1052
 Shibata, S., Tominaga, N., & Tanaka, M. 2014, *ApJ*, 787, L4
 Steinacker, J., Baes, M., & Gordon, K. D. 2013, *ARA&A*, 51, 63
 Stratta, G. et al. 2013, *ApJ*, 779, 66
 Takahashi, H. R., & Ohsuga, K. 2013, *ApJ*, 772, 127
 Takahashi, H. R., Ohsuga, K., Sekiguchi, Y., Inoue, T., & Tomida, K. 2013, *ApJ*, 764, 122
 Tanvir, N. R. et al. 2009, *Nature*, 461, 1254
 Tolstov, A. G. 2005, *A&A*, 434, 623
 Tolstov, A. G., Blinnikov, S. I., & Nadyozhin, D. K. 2013, *MNRAS*, 429, 3181
 Tomida, K., Tomisaka, K., Matsumoto, T., Hori, Y., Okuzumi, S., Machida, M. N., & Saigo, K. 2013, *ApJ*, 763, 6
 Tominaga, N. 2009, *ApJ*, 690, 526
 Turner, N. J., & Stone, J. M. 2001, *ApJS*, 135, 95
 Uehara, T. et al. 2012, *ApJ*, 752, L6
 Vestrand, W. T. et al. 2005, *Nature*, 435, 178
 Woźniak, P. R., Vestrand, W. T., Panaitescu, A. D., Wren, J. A., Davis, H. R., & White, R. R. 2009, *ApJ*, 691, 495
 Yonetoku, D. et al. 2011, *ApJ*, 743, L30
 Yonetoku, D., Murakami, T., Nakamura, T., Yamazaki, R., Inoue, A. K., & Ioka, K. 2004, *ApJ*, 609, 935
 Zhang, B. 2014, *International Journal of Modern Physics D*, 23, 30002
 Zhang, B., & Pe'er, A. 2009, *ApJ*, 700, L65